Applied Organometallic Chemistry

WILEY

Applied Organometallic Chemistry

RESEARCH ARTICLE OPEN ACCESS

Exploring Anticancer Activity and DNA Binding of Metal (II) Salicylaldehyde Schiff Base Complexes: A Convergence of Experimental and Computational Perspectives

Ibrahim Waziri[1] | Sheldon Sookai[2] | Tunde L. Yusuf[3] | Kolawole A. Olofinsan[4] | Alfred J. Muller[1]

[1]Research Centre for Synthesis and Catalysis, Department of Chemical Sciences, University of Johannesburg, Johannesburg, South Africa | [2]Molecular Sciences Institute, School of Chemistry, University of the Witwatersrand, Johannesburg, South Africa | [3]Department of Chemistry, Faculty of Natural and Agricultural Sciences, University of Pretoria, Hatfield, South Africa | [4]Department of Pharmacology, University of Free State, Bloemfontein, South Africa

Correspondence: Ibrahim Waziri (201800230@student.uj.ac.za)

Received: 12 March 2025 | **Revised:** 27 March 2025 | **Accepted:** 31 March 2025

Funding: This work was supported by the South African National Research Foundation (111706 and 116177).

Keywords: cancer | metal complexes | metallodrugs | Schiff base

ABSTRACT

Metal complexes derived from salicylaldehyde-based Schiff bases are among the frontrunners in the pursuit of precise and potent cancer treatments due to their remarkable prowess. In this study, salicylaldehyde-based Schiff base (**HL**) was prepared via a reaction between 2-amino-5-benzonitrile and salicylaldehyde. Subsequently, **HL** was further reacted with Ni (II), Co (II), Cu (II) and Pd (II) ions using their respective metal salts to obtain homoleptic mononuclear complexes (**C1**–**C4**). The composition of **HL** and **C1**–**C4** were determined using ^{1}H and ^{13}C NMR, UV–Vis, FTIR, CHN, SEM–EDX and HRMS analyses. In addition, the structural geometries of **HL**, **C1**, **C3** and **C4** were determined in solid state using single crystal X-ray diffraction analysis and corroborate with the mentioned characterization techniques employed. The stability of compounds was assessed through time-dependent UV–vis spectroscopy, revealing that **C2** exhibited the highest stability under the experimental conditions. Subsequently, the anticancer effects of **HL** and **C2** were tested on breast cancer cell lines (MCF-7) using MTT, LDH and ATP assays. Both **HL** and **C2** displayed potential cytotoxicity on the MCF-7 cell line, in which **C2** displayed a better inhibition effect than a standard chemotherapeutic agent, doxorubicin (DOX), with IC_{50} of 43.08 μM. We postulate that the mechanism by which **C2** may function is by binding to DNA ($K_a = 0.114\ (\pm 0.02) \times 10^4$) and intercalation (shown by UV-CD and UV-LD spectroscopy) at the AT rich sites. These data were corroborated in silico by extra precision (XP) docking and molecular dynamic (MD) simulations.

1 | Introduction

The discovery of cisplatin led to the development of carboplatin and oxaliplatin, which share a similar DNA-binding mechanism, enabling effective tumor cell destruction [1–3]. However, their use is limited due to significant side effects and the emergence of drug-resistance within patients, prompting research into alternative metal-based compounds [4–6]. The effectiveness of such drugs depends on factors like metal oxidation states, ligand structures and metal–ligand interactions [7–9]. Guided by these properties, research in this field has driven the creation of innovative drugs featuring powerful ligands coordinated with a

Ibrahim Waziri and Sheldon contributed equally to this work.

variety of metals, broadening the scope of metallodrugs in cancer therapy [10, 11].

First-row transition metals include structurally characterized Ni (II), [12–14] Pd (II), [14–16] Pt (II), [17–19] Co (II/III), [20–23] Rh(I/II), [24–27] Ir (III), [25, 28] Cu (II), [29–31] Ag(I), [32] and Au (III) complexes [33]. These have gained attention due to their lower toxicity, natural occurrence in the body and established pharmacological effects [34–36]. The activity of their complexes is influenced by the ligands' structural modifications, such as bulky or electron-withdrawing substituents [37–40], which can enhance anticancer efficacy. Additionally, functional group integration in ligands has been pivotal in adjusting cytotoxicity [41, 42]. Schiff bases frequently showcase captivating bioavailability [43–45] and stability characteristics [46–48], fueling extensive research efforts into their synthesis. Schiff bases, known for their coordination capabilities with various metal ions [49, 50], exhibit a wide range of biological effects, including antioxidative [29, 51–53], anticancer [54], antimicrobial [55] and even anti-COVID properties [56]. Among Schiff bases, Salicylaldehyde-based Schiff bases, recognized for their synthesis ease and effectiveness, along with their metal complexes [57, 58], have shown promise as potent anticancer agents, outperforming established controls in various assays [59, 60].

In recent years, a plethora of salicylaldehyde-based Schiff base coordination complexes has emerged as promising contenders for anticancer treatments. For instance, in 2008, Lange et al. [61] scrutinized an octahedral iron (III) complex and assessed its efficacy against SKOV-3 and OVCAR-3 cells using a viability assay (MTS assay) after a 24-h treatment period. Interestingly, the unbound ligand showed no cytotoxic effects, indicating that the compound's anticancer properties primarily stem from the metal core whereas the ligand aids in enhancing drug penetration across lipid cell membranes. Impressively, the coordination complex exhibited a remarkable IC_{50} value of 300 nM, a significant feat considering the resistance of SKOV-3 and OVCAR-3 cancer cells to platinum-based medications [61]. In 2013, Li et al. [62] synthesized the pentacoordinate copper complex, derived from a salicylaldehyde-based Schiff base, characterized by a square pyramidal geometry elucidated through single-crystal X-ray diffraction (SCXRD). The researchers explored the antineoplastic potential of the Schiff base ligand and Cu complex against Hep-G2 cells via the MTT assay following a 24-h treatment regimen. The complex demonstrated noteworthy cytotoxic activity with an IC_{50} value of 13.9 μM, surpassing cisplatin ($IC_{50} = 28.8\,\mu M$) and the free ligand ($IC_{50} = 22.1\,\mu M$). This heightened efficacy was attributed to a robust interaction with DNA, influenced by the complex's geometry and oxidation state [62].

In 2020, Smiłowicz et al. [63] synthesized cobalt (III) complexes based on salicylaldehyde derivatives with a carboxyl group substituted in the aromatic spacer, incorporating various coligands in the *trans* position. The cytotoxicity of these compounds was evaluated against A-549 and Hep-G2 cancer cells and GM5657T noncancer cells using the MTT assay after a 48-h incubation period. The unaltered coordination complexes exhibited moderate activity against A-549 and Hep-G2 cells, with limited selectivity towards GM5657T cells. Notably, the cobalt complex demonstrated slightly higher cytotoxicity ($IC_{50} = 13.2 \pm 0.8\,\mu M$) than cisplatin ($IC_{50} = 13.3 \pm 1.4\,\mu M$) against Hep-G2 cells. In 2012, Asadi et al. [64] synthesized copper (II) and nickel (II) complexes with an aromatic spacer utilizing pyridine instead of benzene for the imino groups. The researchers evaluated the anticancer potential of these compounds against K-562 cancer cells via the MTT assay following a 24-h incubation, yielding notably remarkable cytotoxic results. In 2020, Özdemir et al. [65] investigated the anticancer efficacy of four salicylaldehyde-based Schiff base complexes of palladium (II). These compounds were tested against HeLa and MCF-7 as well as a normal human cell line (HEK-293) using the MTT. All four compounds showed moderate activity against HeLa, and one of the complexes showed higher activity against MCF-7 than the standard control.

Building on these findings, we intended to design a series of novel early-stage investigational drugs that are cytotoxic against MCF-7 cells. Therefore, we designed a novel Schiff base, (E)-2-([2-hydroxybenzylidene]amino)-5-methylbenzonitrile, derived from salicylaldehyde and featuring a cyano group for enhanced cytotoxicity and a methyl group for improved lipophilicity. These structural modifications are intended to disrupt cancer cell membranes [66], enhance cellular penetration and improve receptor interactions [67]. By complexing this Schiff base with Ni (II), Co (II), Cu (II) and Pd (II) ions, we aim to develop potential anticancer agents with improved biological properties. Furthermore, our study emphasizes the importance of stability assessments to ensure the reliability and efficacy of these compounds before cytotoxicity testing.

2 | Results and Discussion

2.1 | Metal Chelate Synthesis and Spectroscopic Characterization

An ON donor substituted Schiff base ligand (**HL**) was synthesized by reacting 2-amino-5-methylbenzonitrile and salicylaldehyde in methanol solvent with formic acid as a dehydrating agent at room temperature. Mononuclear homoleptic complexes of Ni (II), Co (II), Cu (II) and Pd (II) (**C1–C4**) were obtained by reacting the respective metal salts with the ligand (**HL**) in a 1:2 mol ratio of metal to ligand in a refluxing mixture of dichloromethane (DCM) and methanol. The ligand and its complexes (**C1–C4**) were obtained in good yield (65%–76%; Scheme 1) and characterized using various spectroscopic and analytical techniques (ESI Figures S1–S28). **HL**, **C1**, **C3** and **C4** structures were determined through SCXRD analysis.

2.1.1 | NMR Spectroscopy

In the proton (^{1}H NMR) spectrum of the ligand (**HL**), a signal corresponding to the phenolic proton was detected in the 12.46-ppm region. The proton from the azomethine moiety appeared around 9.10 ppm on the spectrum. The presence of these protons in the downfield region of the spectrum aligns with findings from previous studies on salicylaldehyde-based Schiff bases [68, 69]. Additionally, a signal at 2.37 ppm is attributed to the protons of the substituted methyl group. Chemical shifts for the aromatic protons were observed in the range of approximately 6.99–7.72 ppm (Figure S1). Similarly,

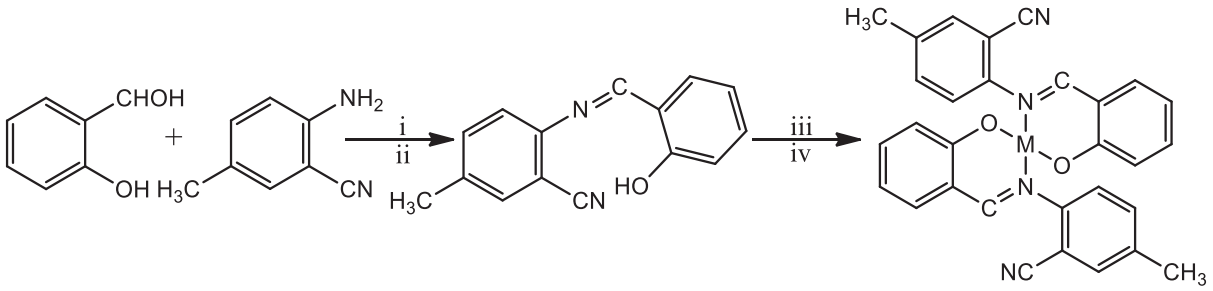

SCHEME 1 | Routes for the synthesis of the ligand (**HL**) and metal complexes (**C1**–**C4**): i = CH_3OH/HCOOH; ii = RT/3 h; iii = $CHCl_2$/CH_3OH; and iv = 65°C/6 h; M = Co (II), Ni (II), Cu (II) or Pd (II) ions.

the ^{13}C NMR spectrum of **HL** (Figure S2) presented signals that accounted for all the carbon atoms in the compound. Notably, a signal due to the substituted methyl group was observed upfield at 20.0 ppm. Similarly, a signal due to the azomethine(C=N) carbon was noted downfield at 164.8 ppm. The signal due to the aromatic carbon was observed at 107.1–160.2 ppm. After coordination with the metal ions and the subsequent formation of the complexes (**C1**–**C4**), significant differences were observed between the spectrum of **HL** and those of the complexes, particularly in the diamagnetic complexes (**C1** and **C4**). One notable change was the disappearance of the signal corresponding to the phenolic proton, which was initially observed at 12.46 ppm in the free ligand. This disappearance can be attributed to the deprotonation and the formation of a bond between the phenolate oxygen and the metal ions.

The signal for the azomethine (HC=N) proton, originally detected at 9.10 ppm in the ligand spectrum, was observed at 9.07 ppm in **C1** and 8.19 ppm in **C4**. This shift indicates an upfield shift compared to the free ligand. The increase in electron density on the azomethine group, resulting from coordination involving the nitrogen atom, causes a shielding effect on the proton, leading to the observed upfield shift [70]. Furthermore, slight changes were also noted in the ^{13}C NMR spectra of **C1** and **C4**. The chemical shifts of the carbon atoms in the complexes exhibited a slight upfield shift in comparison to the ligand. Detailed analysis of the electronic spectroscopy and FT-IR are reported in the Supporting Information.

2.2 | X-Ray Crystal Structures

The structures of **HL**, **C1**, **C3** and **C4** were determined using single-crystal crystallography (Figure 1). The crystal structure of **C3** was found to crystallize in a triclinic *P*-1 space group, whereas **HL**, **C1** and **C4** crystallized in a *C*2/*c* crystal system. In the structure of **HL**, a classical O(1)–H(1)···N(2) hydrogen bond with a distance of 1.895 Å plays a key role in stabilizing the molecule. Further examination of the crystal structure revealed the presence of nonclassical hydrogen bonds, including C(2)–H(2)···N(2) (2.682 Å), C(9)–H(9)···N(2) (2.590 Å) and C(3)–H(3)···N(2) (2.584 Å), which contribute to the formation of a three-dimensional supramolecular network. The bond parameters align with those reported for similar structures in the literature [71]. Notably, the **HL** structure features three C–N bonds: an imine C=N with a bond distance of 1.281 Å, a cyano group at the paraposition of the aniline with a C ≡ N bond distance of 1.140 Å and C–N with a bond distance 1.414 Å. The molecule is planar, exhibiting a torsional angle of approximately 180° around the C(1)-N(1)-C(9)-C (10) linkage (Figure 1a). All the metal complexes contain half of the molecular unit in the asymmetric unit. Each complex is mononuclear, consisting of a single central metal atom and two ligands (Figure 1b–d). The ligands coordinate to the metal centre through the phenolic oxygen and imine nitrogen atoms, adopting a trans configuration. To accommodate this trans arrangement around the metal centre, the dihedral angle of the ligand decreases from 180° to approximately 170°. The bond angles and distances are consistent with those typically observed in mononuclear Schiff base metal complexes, as documented in the literature [58, 72–75]. Further examination of the crystal structures showed no evidence of intramolecular hydrogen bond interactions. However, intermolecular hydrogen bonds were observed. In the **C3** complex, two notable intermolecular interactions are present in the crystal system (Figure S29b). The molecule is stabilized through interactions with neighbouring atoms, specifically C(7)–H(7)···N(1) (2.608 Å) and C(4)–H(4) ···H(12)–C(12). Due to the inability to obtain suitable single crystal for data collection using single-crystal X-ray diffraction (SCXRD) analysis for **C2**, supplementary characterization including scanning electron microscopy (SEM) and energy dispersive X-ray spectroscopy (EDX) were conducted on the compound and compared with the ligand (Figures S6, S18 and S19). The findings from this supplementary assessment of **C2**, combined with the result from mass spectrometry and elemental analysis, affirmed the formation of the compound.

2.3 | Stability of transition metal complexes

The stability of an early stage investigational metallo-drug candidate is important for various reasons, such as if it will remain intact in an aqueous environment. Many metallodrug candidates such as auranofin (Au [I]) and cisplatin (Pt [II]) and NAMI-A (Ru [II]) undergo ligand exchange reactions and ultimately react as a more simple (ionic) metal species both *in vitro* and *in vivo* [76, 77]. The stability of the Co (II) complex **C2** was evaluated in a phosphate buffer (10% [v/v]) DMF as a function of time by spectroscopy in the UV–visible region (Figure 2a). The spectral changes indicated that **C2** is relatively stable over a 36-h time frame in a phosphate buffer (Figure 2a). There are no observed chemical changes such as metal ion release or bond dissociation observed over the 36-h time period. Furthermore, there were no isosbestic points

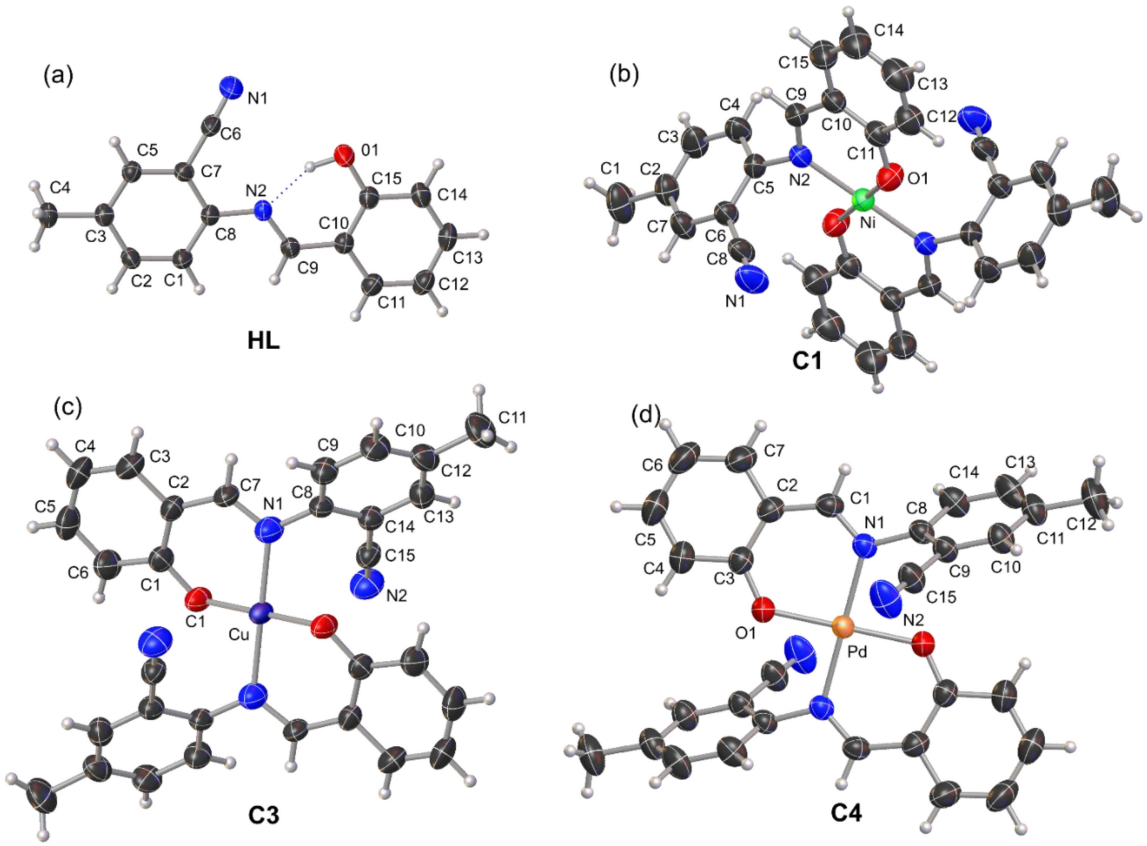

FIGURE 1 | (a) Labelled view of the low temperature X-ray structure of **HL**. (b) Labelled view of the X-ray structure of **C1**. (c) Labelled view of the X-ray structure of **C3**. (d) Labelled view of the X-ray structure of **C4**. Thermal ellipsoids are rendered at 50% for all complexes. Hydrogen atoms are drawn as spheres with an arbitrary.

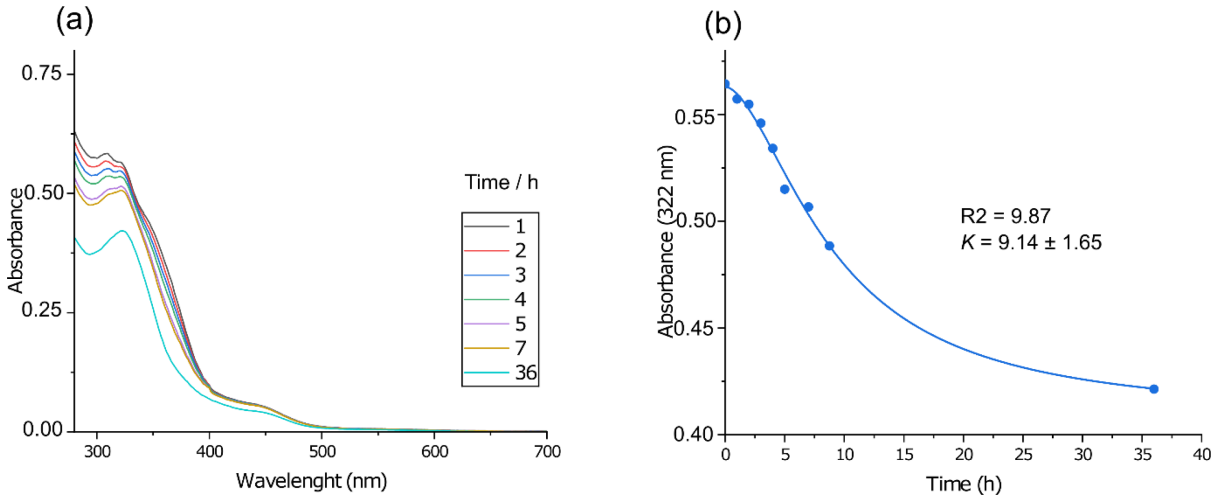

FIGURE 2 | UV–vis spectra of 30-μM solutions of (a) **C2** recorded as a function of time in KH_2PO_4 buffer (50 mM pH 7.5). **C2** was present with a final concentration of 10% (v/v) DMF.

observed in the spectra, indicating that **C2** had not undergone any chemical reaction within the investigated time interval and that the decrease in absorption over the 36 h is likely a gradual, partial precipitation of the **C2**. The kinetics of the precipitation of **C2** (monitored at 322 nm) indicated that the process was first order ($t\frac{1}{2} = 9.14 \pm 1.65$ h) as shown in Figure 2b. Over the 36-h period, there was 75% of the intact **C2** complex in solution suggesting that it will make a suitable investigational drug candidate to test further. The other transition metal complexes' stability was also evaluated in a phosphate buffer (10% [v/v] DMF) as a function of time by spectroscopy in the UV–visible region (Figure S30) and was found not to be suitably stable. In the case of **C4**, the absence of isosbestic points was noted; however, the decrease in absorbance is

more pronounced, suggesting rapid precipitation of the complex. Based on the spectral data, we cannot confirm whether demetallation is occurring. In contrast, compounds **C1** and **C3** demonstrate rapid demetallation, evidenced by the disappearance of the metal absorption band at ~425 nm. Considering the spectral data, only **C2** was deemed suitable for further analysis.

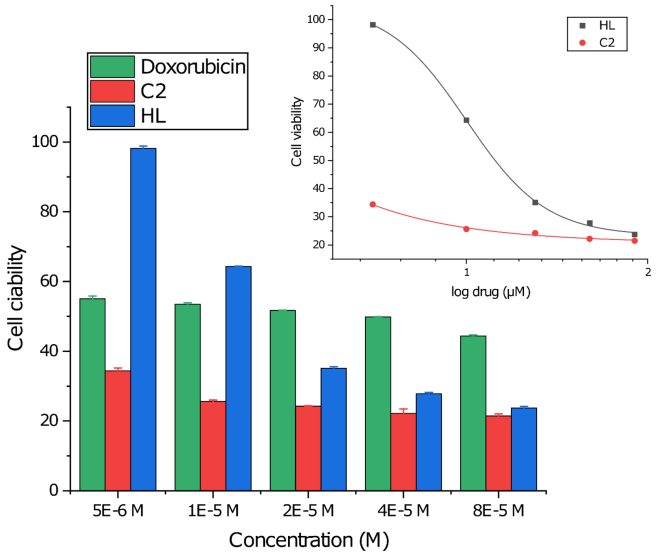

FIGURE 3 | Relative cell viability graphs represent the changes in cell viability percentage of MCF-7 cells in response to treatment with increasing concentrations of **Dox**, **C2** and **HL** relative to a vehicle control. Error bars represent standard deviation ($n = 3$). Insert represents cell viability percentage MCF-7 cells in response to treatment with increasing concentrations of complexes **HL** and **C2** fitted with a Hill fit plot to delineate the IC_{50} concentrations.

TABLE 1 | IC_{50} values of **HL**, **C2** and **Dox** on MCF-7 cells.

Compounds	IC_{50} (μM)
HL	39.78
C2	< 5
Dox	48.03

2.4 | Cell Cytotoxicity

Following the stability study on the metal complexes **C1**–**C4** (Figures 2a and S30), which revealed that only **C2** remained stable in an aqueous medium, **C2** was assessed for its antiproliferative activities on the hormone-responsive breast cancer cell line MCF-7 using 3-(4,5-dimethylthiazol-2-yl)–2,5-diphen yltetrazolium bromide (MTT). This was compared to **HL** and the control Doxorubicin (**Dox**). The MCF-7 cells were treated with the respective drugs at concentrations ranging from 5 to 80 μM (Figure 3). It is evident that the activity depends on the metal ion centre in **C2** because it exhibited higher cytotoxicity compared to **HL** and Doxorubicin. Both **C2** and **HL** show a dose-dependent reduction of cell viability of MCF-7 cells, with **C2** being more potent than both the free **HL** and **Dox**. The IC_{50} values for **HL**and **Dox** were found to be 39.78 and 48.03 μM (Table 1), whereas the IC_{50} for **C2** could not be delineated from the current data set as the IC_{50} would be below the lowest concentration used (5 μM). Similar cytotoxic activity was observed for a series of novel lanthanide salicylaldehyde-based complexes (i.e., praseodymium, erbium and ytterbium) that were tested against MCF-7 cells [78] and Zn (II) and Ni (II) salicylaldehyde-based Schiff bases [79].

Microscopic images of MCF-7 cells control cells before and after treatment of **C2** (5 μM) for 24 h are provided in Figure 4. The MCF-7 cells before treatment with **C2** (Figure 4a) consisted of irregular confluent combined with smooth-edged polygonal structures and indicated several cell surface protuberances. The cell grew rapidly with a skeleton-like structure. Following administration of 5 μM of **C2** for 24 h, the MCF-7 cell volume and density decreased (Figure 4b). The reduced cell viability is likely due to **C2**, binding to the adenosine-thymine

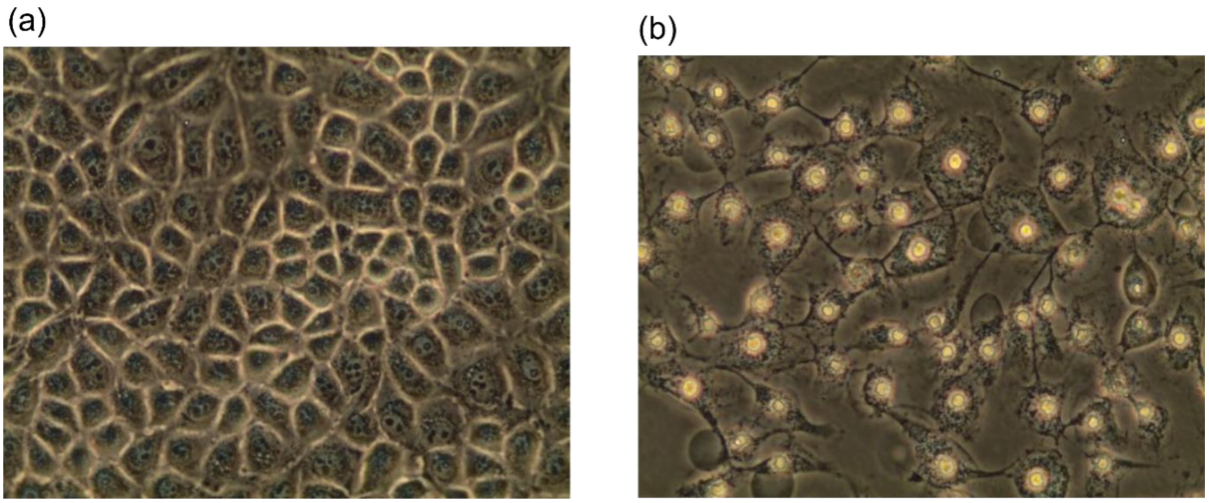

FIGURE 4 | (a) Morphology of MCF-7 cells before treatment of any drug. (b) Morphological changes in MCF-7 cells induced by complex **C2** (5 μM). Control drug **HL** and **Dox** morphological changes on MCF-7 cells are presented in Figure S29. Captured using Wirsam Olympus inverted light microscope (CKX 41) equipped with Olympus C5060-ADUS digital camera at 400X magnification.

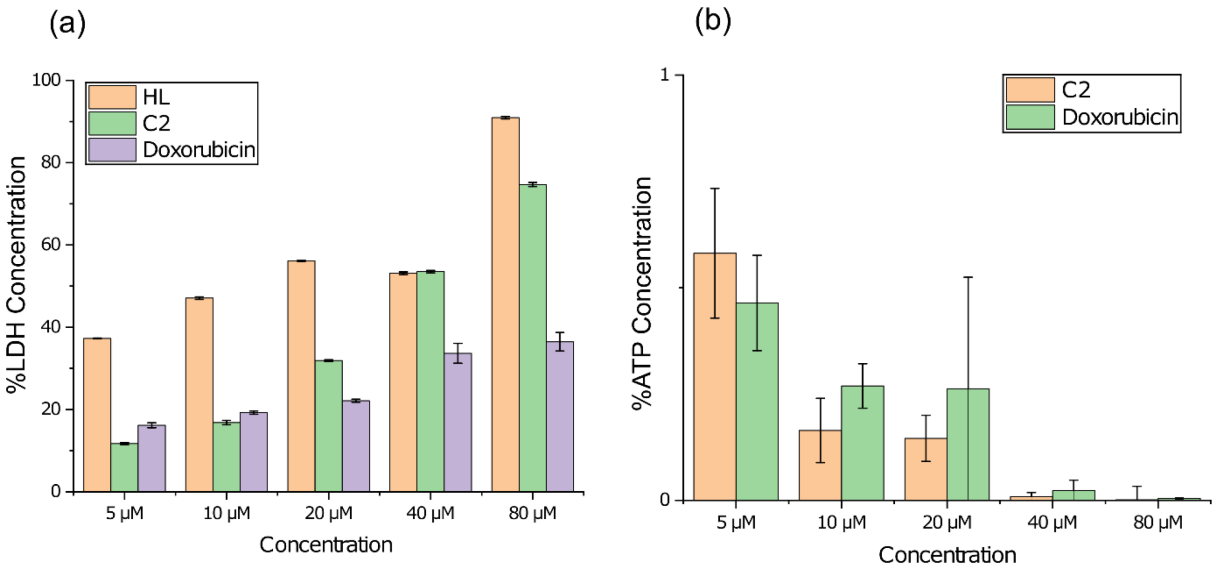

FIGURE 5 | Plot of the compound-induced cytotoxicity in MCF-7 cells: LDH activity (a) and changes in ATP levels (b).

(AT) pockets within the DNA strand (*vide infra*) and intercalating with the DNA. This results in inhibited DNA replication and, ultimately, apoptosis of the cells [80–82]. **Dox** was specifically used as a control drug due to its speculated activity to bind to and intercalate with DNA [81], similar to complex **C2** (*vide supra*). Therefore, reduced cell viability was observed for MCF-7 cells in the presence of both **C2** (Figure 4b) and **Dox** (Figure S31).

Lactate dehydrogenase (LDH) is a cytoplasmic enzyme that catalyses the conversion of lactate to pyruvate, simultaneously reducing NAD^+ to NADH. The release of LDH serves as a marker for cell damage because, during apoptosis, the disruption of the plasma membrane causes LDH to leak from the cytoplasm into the extracellular environment. Consequently, LDH activity is widely used as an indicator of cytotoxicity. The *in vitro* cascade of reactions used to assess a drug's cytotoxic effects relies on the production of $NADH/H^+$, which is acted upon by diaphorase. Diaphorase transfers H^+/H^+ from NADH to the tetrazolium salt INT (2-[4-iodophenyl]-3-[4-nitropheny l]-5-phenyltetrazolium chloride), reducing it to red formazan dye, which can be quantitatively detected [83, 84]. **C2**, **HL** and **Dox** all exhibited increased LDH activity in a dose-dependent manner, as expected. However, unexpectedly, MCF-7 cells treated with **HL** showed the highest LDH activity despite **HL** having lower cytotoxicity compared to both **Dox** and **C2** (Figure 5a). These results suggest that **C2** may interfere with the LDH activity assay. Metal complex drugs are known to interfere with LDH assays by binding to the enzyme itself [85, 86]. To investigate this possibility for **C2**, we conducted an in silico XP docking study (Figure S32), which revealed that the best-docked pose of **C2** is bound to the NAD^+/H^+ site. We propose that the elevated LDH activity observed in MCF-7 cells treated with **HL** is due to **C2** inhibiting extracellular LDH activity, leading to lower measured enzyme activity, which does not reflect the true amount of LDH present. Now, due to the reduced LDH, diaphorase cannot effectively transfer H/H^+ from NADH to the tetrazolium salt INT and allow it to be reduced to formazan. One of the most well-known metallodrugs reported to inhibit LDH activity through an unknown mechanism is cisplatin [85]. The ATP assay determines the amount of adenosine triphosphate produced by living cells. In the case of the ATP assay, both compounds demonstrated dose-dependent toxicity, with **C2** inducing a notable reduction in ATP levels, particularly at higher concentrations (Figure 5b). The substantial decrease in ATP levels suggests that **C2** inhibits MCF-7 cell growth, induces cell death and disrupts their metabolic pathways, further solidifying **C2** as a more potent cytotoxic agent.

2.5 | Density Functional Theory (DFT) Study: Optimization Energy and Optimized Geometry

Simulations using density functional theory (DFT) were performed to further investigate the electrostatics, solid-state structures and electronic structures of the metal complexes **C1**, **C3**, **C4** and **HL**. Optimization and frequency calculations were conducted using Gaussian 16 W [34] at the CAM-B3LYP/DEF2-QZVP/GD3BJ level of theory. The input files were prepared using the single-crystal structures of each molecule in Gauss View 6.0 [35], which was also used to analyse the output files.

Geometry optimizations and frequency calculations were performed on the free ligand and all four metal complexes (**C1**–**C4**). The absence of negative Eigen values indicates that the geometry optimizations successfully identified true minima on the global potential energy surface. Structural overlays (least-squares fits) of the X-ray structures and DFT-calculated structures were used to compare deviations within the structures (using Mercury 3.1 [36]). The root mean square deviations (RMSDs) showed that the X-ray and DFT-simulated structures are in excellent agreement (Figure 6). Interestingly, the metal complexes **C1** and **C4** exhibited almost zero RMSD deviations. A summary of selected bond lengths and bond angles is reported in Table 2, to further highlight the accuracy of the DFT simulated structures in relation to the X-ray structures.

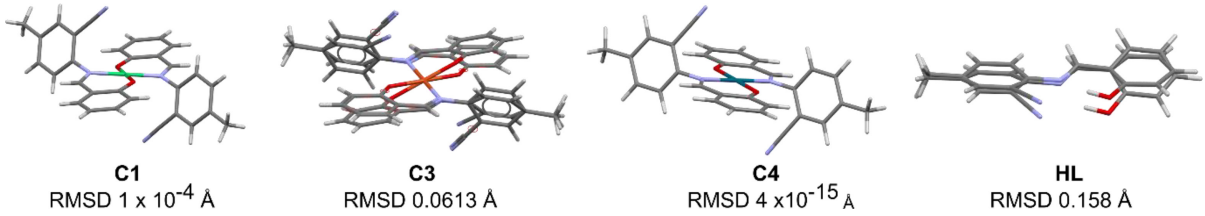

FIGURE 6 | Comparison of DFT-calculated and X-ray crystal structures of **C1**, **C3**, **C4** and **HL**. Root mean square deviations (RMSDs) for all atoms for each structure are indicated on the diagram (Å).

TABLE 2 | Selected crystallographic and DFT-calculated bond distances and bond angles for **C1**–**C4** and **HL**.

Bond distance (Å)	C1[a]		C2[b]		C3[a]		C4[a]		HL[a,c]	
	X-ray	DFT	X-ray	DFT	X-ray	DFT	X-ray	DFT	X-ray	DFT
M-N	1.912 (16)	1.913	ND	1.945	2.008 (2)	2.006	2.017	2.030	NA	NA
M-O	1.820 (15)	1.825		1.841	1.890 (19)	1.887	1.964 (15)	1.987	NA	NA
C=N	1.434 (2)	1.313		1.312	1.426 (3)	1.313	1.434 (3)	1.311	1.400 (3)	1.304
C-N	1.304 (3)	1.444		1.444	1.298 (3)	1.437	1293 (3)	1.440	1.272 (3)	1.414
C-O	1.310 (2)	1.323		1.330	1.302 (3)	1.322	1.301 (3)	1.325	1.338 (3)	1.359
Bond angles (°)	**X-ray**	**DFT**	**X-ray**	**DFT**	**X-ray**	**DFT**	**X-ray**	**DFT**	**X-ray**	**DFT**
O-M-N_{cis}	92.68	92.79	ND	91.93	90.93	91.21	92.34	91.80	NA	NA
N-M-N	180	179.99		179.99	180	179.97	180	179.99	NA	NA
O-M-O	180	179.99		179.98	180	179.98	180	179.97	NA	NA
C=N-C	115.51	115.55		115.66	116.74	116.72	117.65	117.51	121.60 (2)	122.17

[a]Standard uncertainty is provided in parenthesis.
[b]Crystal structure for molecule not determined.
[c]Bond length or bond angles are not applicable for this molecule.

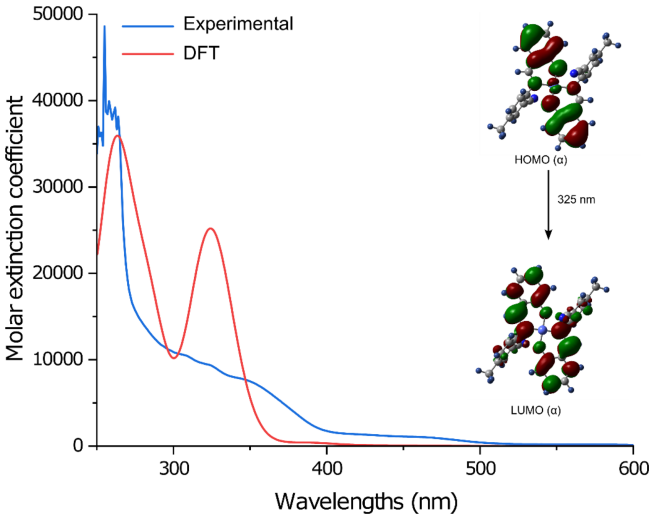

FIGURE 7 | The experimental and DFT calculated UV–vis spectra of **C2** as well as 60 excited singlet state transitions. The dominant electronic transition responsible for the visible colour of the **C2** solution was calculated and observed at 325 nm.

The finding from Figure 6 and Table 2 strongly suggests that the CAM-B3LYP/DEF2-QZVP/GD3BJ level of theory can reliably optimise the structure of **C2**, for which a single crystal could not be obtained. The optimized structure of **C2** will subsequently be used in molecular dynamics (MD) simulations to predict the theoretical mode of binding of **C2** to DNA (*vide infra*).

Analysis of frontier molecular orbital (FMO) maps and molecular electrostatic potential (MEP) maps are reported in the Supporting Information at the 3-21G basis set (Figures S35–37 and Tables S6 and S7).

2.6 | Electronic Spectroscopy

The experimental UV–vis spectrum of **C2** is presented in Figure 7 and was assigned by analysis of the DFT-calculated spectrum of the complex. The DFT-calculated electronic spectrum of **C2**, which excludes vibronic transitions, is in excellent agreement with the experimental spectrum, and no correction in the wavelength was needed. In contrast **C1**, **C3** and **C4** required wavelength scaling corrections of 70, 30 and 40 nm, respectively. The visible band at 325 nm (first excited electronic state) is decomposed into the following major contributions HOMO (α)->LUMO(α) (28%), H-1(β)->LUMO(β) (23%), HOMO(β)->L+1(β) (30%) H-1(α)->L+1(α) (6%), H-1(β)->L+3(β) (2%). The dominant contribution HOMO(α)->LUMO(α) has been shown in Figure 7, and this π-π* transition involves mostly ILCT (intra

ligand charge transfer) with some ligand-to-metal character. The higher energy transitions at 283-nm major contributions were H-2(α)->LUMO(α) (14%), H-2(β)->L+1(β) (24%) H-6(α)->L+1(α) (7%), H-4(α)->LUMO(α) (4%) and H-1(α)->L+8(α), whereas the 268-nm band major contributions were H-1(α)->L+1(α) (25%), HOMO(α)->LUMO(α) (11%) H-12(α)->LUMO(α) (3%), H-11(α)->LUMO(α) (6%), H-4(α)->LUMO(α) (6%), H-2(α)->LUMO(α). These high-energy LUMOs are metal-based and have mostly σ* character. Hence, the absorption at 268 nm is a π-σ* transition with significant ligand-to-metal charge transfer. The data presented in Figure 7 further corroborated that the experimental data are in excellent agreement with the theoretic TD-DFT data, suggesting we have the right complex in **C2**. Assignments of the TD-DFT of **C1**, **C3** and **C4** are presented in Figures S32–34 and Tables S2–S5.

2.7 | Complex C2 Binding to ctDNA

The transition metal complexes in this study were designed to target DNA as their mode of action, serving as early-stage investigational compounds for cancer treatment. However, only **C2** proved to be sufficiently soluble and stable for these actions. Due to the planar structure of **C2**, it is anticipated that the compound will bind to and intercalate into DNA. This was tested by measuring the binding constants (K_a), for **C2** to calf thymus DNA (ctDNA) through UV–visible spectroscopic titrations. The absorption maximum for **C2** at 305 nm was monitored, and changes in the electronic spectrum at this wavelength indicate the interaction of **C2** with ctDNA (Figure 8). The highest obtained ratio of [ctDNA]:[**C2**] before the spectrophotometer could no longer detect accurate absorbance readings was 1:3.6.

As shown in Figure 8a, there is a decrease in absorbance intensity across the spectrum, accompanied by a red shift of 4 nm. The red-shift suggests that **C2** is positioned in a more polar environment (i.e., indicating binding to DNA). The decrease in absorbance at 305 nm during the titration with ctDNA was fitted to the Hill model [87] yielding an R^2 value of 0.998 (Figure 8b). Using the Hill model, the affinity of **C2** to ctDNA was quantified by calculating the mean binding constant (K_a) from three independent experiments: $0.114\ (\pm 0.02) \times 10^4$ M.

Typically, the K_a values of groove, binders are marginally higher than those of intercalators, with K_a values ranging from 10^5 to $10^8\ M^{-1}$ [88, 89]. We compared the binding constants to those of other complexes that have been shown to interact with ctDNA. CoSF (CoSF = N,N0 -bis{5-[(triphenylphosphonium chloride)-methyl] salicylidine}-o-phenylenediamine), Co (II), is a water-soluble Co (II) Schiff base chelate that was found to interact with ctDNA by electrostatic interactions and a K_a of 5×10^4 M [90] and a series of Co (II),N-bis (pyridin-2-ylmethyl)aniline complexes, which had a K_a of $1.34–2.04 \times 10^4$ M [91]. **C2** compared favourably with both molecules in terms of similar binding affinities to ctDNA but had significantly lower affinity than a series of mononuclear cobalt (II) complexes containing ligands with extended planar quinoxaline moieties such as {dipyrido[3,2-a:2′,3′-c]phenazine (dppz) or dipyrido[3,2-d:2′,3′-f]quinoxaline (dpq)}, whose K_a values ranged from 0.79 to 3.79×10^5M [92]. Overall, the K_a of **C2** falls in the lower range of binding affinities to ctDNA for known Co complexes.

2.8 | UV-CD and UV-LD Spectroscopy of Complex C2 Binding to ctDNA

UV-CD spectroscopy was employed to visualize the conformational changes of ctDNA in the presence of **C2** (Figure 9a). Native B-form DNA exhibits four major transition bands at 210, 220, 244, and 277 nm. These transitions serve as markers for the double-helical B-conformation of DNA [93, 94]. The maxima's band at 220 and 277 nm is attributed to base stacking, whereas the minima bands at 210 and 244 nm are associated with the helicity of DNA [93, 95]. Upon the addition of the **C2** to the B-form

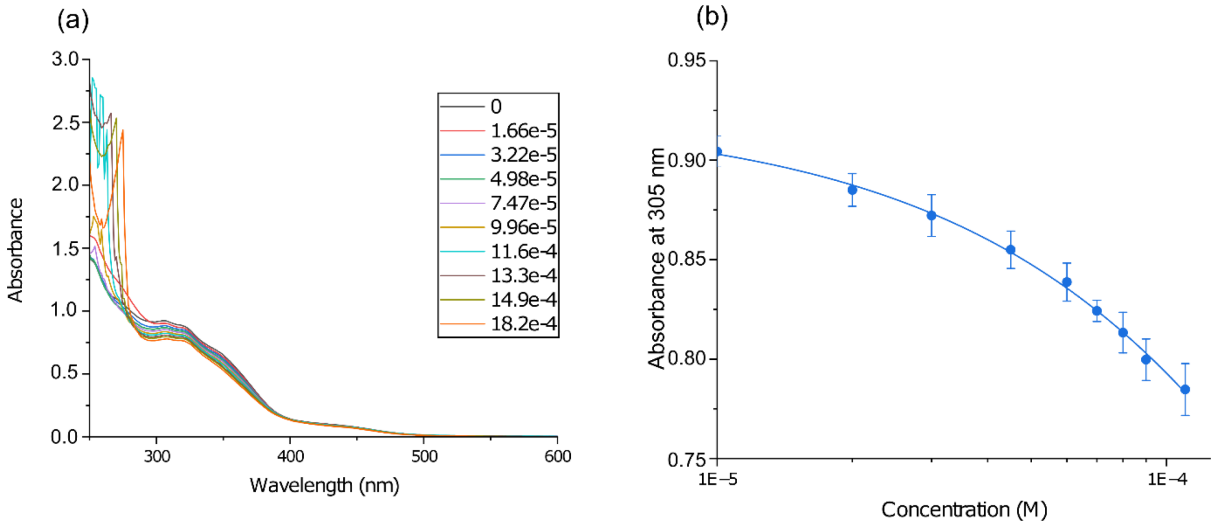

FIGURE 8 | (a) The UV–vis absorption spectra of **C2** (50 μM) and (b) the change in the absorbance at 305 nm of **C2** as a function of [ctDNA] fitted to the Hill model. The reaction was carried out in KH_2PO_4 (10% [v/v] acetonitrile, 50 mM, pH 7.5), and after sequential additions of ctDNA (final [ctDNA] = 182 μM bp), the Hill fits were used to calculate the dissociation constants and stoichiometric ratios for the binding of **C2** to ctDNA. Error bars indicate standard deviation of triplicate data.

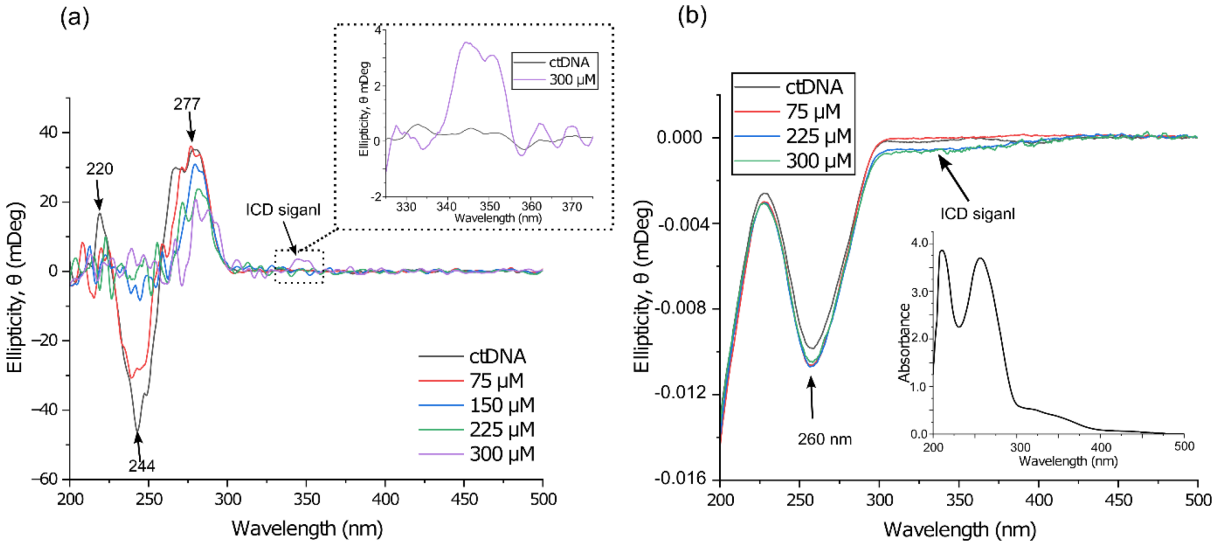

FIGURE 9 | (a) The CD spectrum of **C2** with 100 μM of ctDNA at increasing **C2** concentrations in KH_2PO_4 (10% (v/v) acetonitrile, 50 mM, pH 7.5) at 37°C. The maxima and minima from 210–277 nm represent ctDNA, and the 350-nm band represents an induced CD band due to the interaction of **C2** with ctDNA. (b) The LD spectrum of **C2** with 100 μM of ctDNA at increasing **C2** concentrations in KH_2PO_4 (10% [v/v] acetonitrile, 50 mM, pH 7.5) at 37°C. The minimum at 260 nm represents ctDNA, and the 300–400 nm broadened band represents an induced **C2** LD spectrum.

DNA, the intensities of all four bands decreased, with minimal wavelength shift, indicating DNA condensation in the presence of **C2**. Additionally, the observed changes in the peak intensities were not indicative of a conversion from B-form DNA to the A-form DNA but rather attributed to the aggregation effect of **C2** on ctDNA [96]. It is noteworthy that the A-form of DNA exhibits a maximum peak at 263 nm, and the presence of an ICD signal ~350 nm further emphasizes the binding of **C2** to ctDNA.

All LD experiments were performed in KH_2PO_4 buffer (10% (v/v) acetonitrile, 50 mM, pH 7.5), with ctDNA and varying **C2** concentrations (0–300 μM). The LD spectrum of the ctDNA displays a strong negative signal at 260 nm due to the contribution of the ctDNA nucleotides (purine and pyrimidine base pairs) [97]. Upon the addition of **C2**, a concentration-dependent increase in the amplitude of the 260-nm minima was observed (Figure 7b). This is associated with increasing DNA rigidity (i.e., DNA stiffening), signifying either lengthening and/or an increase in the rigidity of double-helical DNA. The result signifies that DNA is being intercalated and, therefore, being unwound (Figure 9a) [98–100]. Furthermore, an induced dichroic signal appears between 300 and 400 nm. At this spectral wavelength, no contribution from DNA base pairs can be detected, and only the chromophore C2 is absorbed in this region. The inset in Figure 9b highlights the UV–vis spectrum of **C2** and illustrates that the ICD signal absorbs similarly. **C2** is isotropic and cannot be orientated in the flow field. Therefore, the ICD signal suggests that **C2** forms a molecular complex with ctDNA, becomes orientated and is an intercalator of DNA. The ICD signal is below the plane of the native ctDNA, therefore indicating that **C2** is intercalating ctDNA (Figure S35).

2.9 | Molecular Docking and Molecular Dynamic Simulations

Docking studies using Glide XP were employed to corroborate the experimental data (*vide supra*) and potentially demonstrate that complex **C2** binds to and intercalates with DNA. Because rigid X-ray structures of DNA, PDB: 425D (2.80 Å) [101] and PDB: 4E1U (0.92 Å) [102], were used as targets for flexible ligand docking, such methods provide primarily approximate insights into how the metal complex might interact with the target. Notably, docking scores typically do not correlate quantitatively with experimental binding or thermodynamic data (K_a or ΔG values) [103, 104], because docking alone does not try to emulate a physical reaction between the macromolecule and the incoming ligand in the solution. Therefore, only qualitative comparisons are drawn between this data. The in silico data XP glide molecular docking experiments complement the experimental findings from the binding affinity K_a value and observed UV-CD data. The key trends are enumerated below.

TABLE 3 | Summary of GLIDE XP docking scores and selected interaction energy parameters for DNA targets prepared from ligand-free structures derived from PDB codes 425D (biased towards groove binding), 4E1U (biased towards intercalating). The docking runs were truncated to report only the top-scoring ligand pose for each ligand. All energies are in units of kcal mol^{-1}.

PDB	Binding site residues	XP Gscore	Glide energy
PDB: 425D	AT	0.697	−43.872
PDB: 4E1U	AT	−5.473	−57.256

Due to the repeating AT and GC regions in DNA, multiple potential binding sites exist within the molecule. However, because the crystal structures of DNA retrieved from the PDB are rigid and have been crystallized in the presence of either a groove binder (PDB: 425D) or an intercalator (PDB: 4E1U), the binding scores for complex **C2** can be used as a theoretical approach to support experimental data and suggest how complex **C2** interacts with DNA.

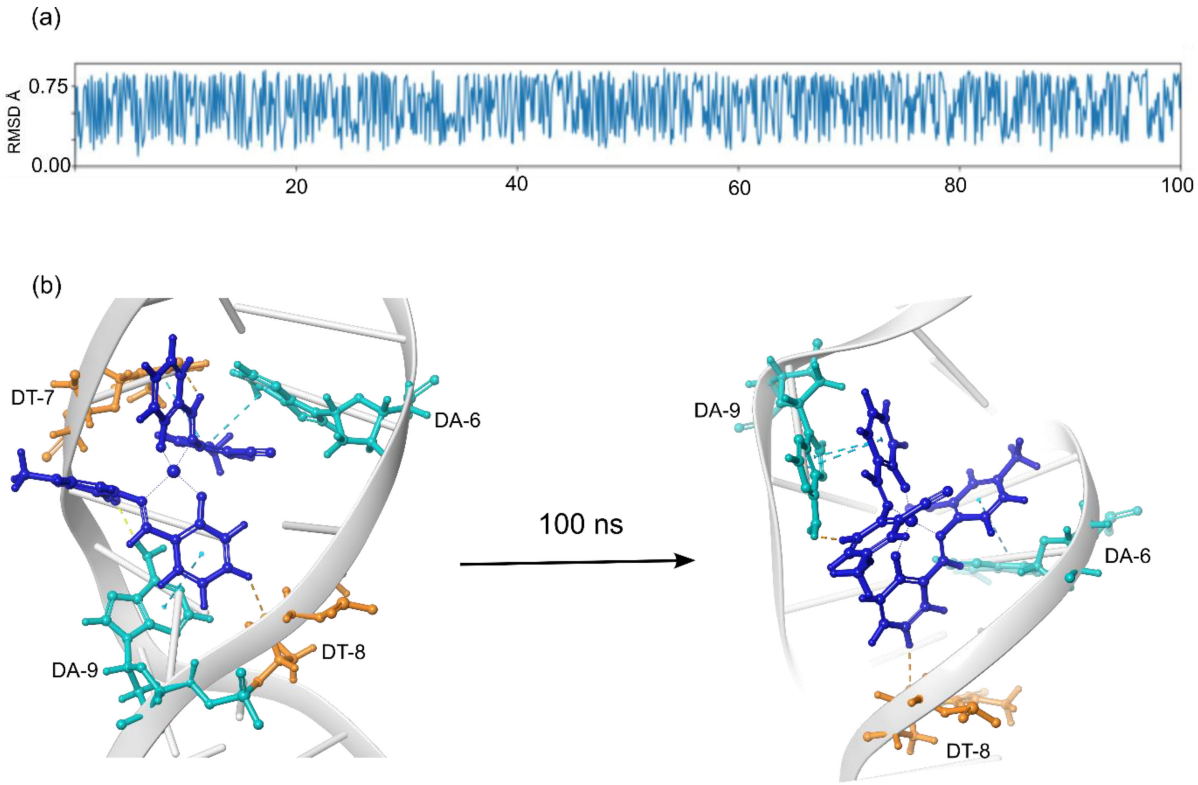

FIGURE 10 | Molecular dynamic simulation (MD) over 100 ns of the best docked GLIDE XP structure of complex **C2** binding to an oligonucleotide of DNA (PDB 4E1U; 5′-D [CGGAAATTACCG]-3′ bound with a cationic ruthenium complex [Ru (bpy)$_2$(dppz)]$^{2+}$) [102]. A large target grid was generated for ligand docking at the [Ru (bpy)$_2$(dppz)]$^{2+}$) site close to the centre of the DNA (with [Ru (bpy)$_2$(dppz)]$^{2+}$) removed), spanning 40×40×40 Å^3, thereby facilitating a search of alternative binding packets radiating throughout the oligonucleotide. (a) The RMSD indicates that there is minimal fluctuation of complex **C2** throughout the MD run, indicating that complex C2 remains bound within the best XP-docked site. (b) Complex **C2** binds within two AT pockets (adenosine shown in teal and thymine shown in orange) and remains in the same site throughout the 100-ns simulation.

XP docking of complex **C2** to both oligonucleotide DNA strands reveals that complex **C2** prefers PDB 4E1U (Table 3), as it exhibits a more favourable ΔG_{bind} score as compared to PDB 425D. This finding corroborates our experimental data (*vide supra*), indicating that complex **C2** binds to and intercalates with DNA. Additionally, the XP docking results suggest that **C2** may bind and intercalate at the central 5′-AT-3′ step of the oligonucleotide (Figure S38), though with a relatively low Glide docking score ($\Delta G_{bind} = -5.47$ kcal/mol). It is unsurprising that AT sites are the preferred binding locations, as they have been shown to exhibit the lowest binding energy [33]. The ΔG_{bind}score for **C2** with the PDB: 425D oligonucleotide was positive, indicative of unfavourable binding, further suggesting that **C2** does not groove bind to DNA.

Following Glide XP docking of complex **2** to the DNA oligonucleotide (PDB: 4E1U), we conducted 100-ns molecular dynamics (MD) simulations (Figure 10) to assess whether the best XP docking pose (Figure S38) was accurately predicted. MD simulations provide insights into the interactions between macromolecules and ligands over time, capturing the dynamic nature of the system and better reflecting physiological conditions [105]. As shown in Figure 10a, the root-mean-square deviation (RMSD) of **C2** remains relatively stable throughout the simulation. Due to the limitations of the Maestro Suite, DNA-specific RMSD and root-mean-square fluctuation (RMSF) values could not be computed, necessitating reliance on the trajectory output to infer ligand binding. Figure 8b illustrates that upon binding, the planar aromatic rings of **C2** insert between two AT-rich pockets—DT(7)–DA(6) and DA(9)–DT(8)—suggesting an intercalation mechanism. This interaction results in the displacement of stacked base pairs and initiates DNA unwinding [106]. At the end of the 100 ns simulation, the DNA structure undergoes significant unwinding, and the electrostatic interaction between **C2** and DT(7) is disrupted (Figure 10b). These MD simulation results align with the experimental data from the UV-LD experiment shown in Figure 8b, where the increase in the 260-nm minimum amplitude is indicative of ctDNA unwinding as a function of **C2** concentration.

3 | Conclusions

In this study, four transition metal complexes (C1-C4) of Ni (II), Co (II), Cu (II) and Pd (II) derived from a salicylaldehyde-based Schiff base ligand (HL) were successfully synthesized and characterized. The molecular structures of HL, C1, C3 and C4 were confirmed through single-crystal X-ray diffraction analysis. A stability assessment revealed that only C2, the Co (II)-derived complex, remained chemically unchanged during the study period. Subsequent cytotoxicity evaluations conducted on C2 and HL, in comparison to Doxorubicin, against the MCF-7 breast cancer cell line demonstrated that C2 exhibited superior cytotoxicity with an IC_{50} below 5 μM, whereas Doxorubicin showed an IC_{50} value of 48.03 μM. The cytotoxic mechanism of C2 was primarily attributed to its DNA-binding and intercalating

capabilities, inhibiting DNA replication and inducing apoptosis. In silico molecular dynamics simulations further supported these findings by illustrating C2's intercalation between AT-rich DNA segments. Additionally, Density Functional Theory (DFT) studies provided valuable insights into the electronic properties of the complex.

Author Contributions

Ibrahim Waziri: conceptualization, methodology, writing – editing original draft. **Tunde L. Yusuf:** conceptualization, formal analysis, review. **Sheldon Sookai:** conceptualization, methodology, writing – editing the original draft. **Kolawole Olofinsan:** formal analysis, writing – review of the draft manuscript. **Alfred J. Muller:** resources, supervision, funding acquisition.

Acknowledgments

Dr. I. Waziri would like to express their gratitude to the URC for awarding the Postdoctoral Research Fellowship (PDRF). The authors also extend their thanks to the South African National Research Foundation (NRF) for providing funding support through Grant No. 111706 to cover running expenses and the Centre for Synthesis and Catalysis of the Department of Chemical Science, University of Johannesburg. The authors thank WITS University and the NRF for funding to purchase a JASCO J-1500 MCD spectrometer (Grant No. 116177, OQM). We also thank the Centre for High-Performance Computing (Project CHEM1633, CHPC, CapeTown) for both the CPU/GPU time and resources needed for the DFT and MD simulations.

Conflicts of Interest

The authors declare no conflicts of interest.

Data Availability Statement

The data that support the findings of this study are available from the corresponding author upon reasonable request.

References

1. M. G. Ferraro, M. Piccolo, G. Misso, R. Santamaria, and C. Irace, "Bioactivity and Development of Small Non-Platinum Metal-Based Chemotherapeutics," *Pharmaceutics* 14 (2022): 954.

2. R. L. Lucaciu, A. C. Hangan, B. Sevastre, and L. S. Oprean, "Metallo-Drugs in Cancer Therapy: Past, Present and Future," *Molecules* 27 (2022): 6485.

3. S. Shruthi and K. Bhasker Shenoy, "Cisplatin Resistance in Cancer Therapy: Causes and Overcoming Strategies," *ChemistrySelect* 9 (2024): e202401449, https://doi.org/10.1002/slct.202401449.

4. Z. Lv, A. Ali, C. Zou, et al., "Salicylaldehyde-Derived Piperazine-Functionalized Hydrazone Ligand-Based Pt (II) Complexes: Inhibition of EZH2-Dependent Tumorigenesis in Pancreatic Ductal Adenocarcinoma, Synergism with PARP Inhibitors and Enhanced Apoptosis," *Dalton Transactions* 53 (2024): 13871–13889.

5. A. Casini and A. Pöthig, "Metals in Cancer Research: Beyond Platinum Metallodrugs," *ACS Central Science* 10 (2024): 242–250, https://doi.org/10.1021/acscentsci.3c01340.

6. Y. Gou, G. Huang, J. Li, F. Yang, and H. Liang, "Versatile Delivery Systems for Non-Platinum Metal-Based Anticancer Therapeutic Agents," *Coordination Chemistry Reviews* 441 (2021): 213975.

7. E. Boros, P. J. Dyson, and G. Gasser, "Classification of Metal-Based Drugs According to Their Mechanisms of Action," *Chem* 6 (2020): 41–60.

8. J. Karges, R. W. Stokes, and S. M. Cohen, "Metal Complexes for Therapeutic Applications," *Trends in Chemistry* 3 (2021): 523–534.

9. P. T. Kaye, "Designer Ligands: The Search for Metal Ion Selectivity," *South African Journal of Science* 107 (2011): 1–8.

10. J. B. Aitken, A. Levina, and P. A. Lay, "Studies on the Biotransformations and Biodistributions of Metal-Containing Drugs Using X-Ray Absorption Spectroscopy," *Current Topics in Medicinal Chemistry* 11 (2011): 553–571.

11. R. K. Sodhi and S. Paul, "Metal Complexes in Medicine an Overview and Update From Drug Design Perspective," *Cancer Therapy & Oncology International Journal* 14 (2019): 25–32.

12. C. H. Wei and J. R. Einstein, "Structure of a Bis-Bidentate Metal Complex, Bis-(N-t-Butylpyrrole-2-Carbaldimino)Nickel (II). Analysis of Its Configurational Disorder in the Crystalline State," *Acta Crystallographica. Section B* 28 (1972): 2591–2598, https://doi.org/10.1107/S056774087200651X.

13. Y. Wang, H. Fu, F. Shen, et al., "Distinct M and P Helical Complexes of H2O and Metal Ions NiII, CuII, and ZnII With Enantiomerically Pure Chiral Bis (Pyrrol-2-Ylmethyleneamine)Cyclohexane Ligands: Crystal Structures and Circular Dichroism Properties," *Inorganic Chemistry* 46 (2007): 3548–3556, https://doi.org/10.1021/ic062316z.

14. S. Bhikraj, O. Q. Munro, and M. P. Akerman, "An Unusual Asymmetric Pseudomacrocyclic Free Base Ligand and Nickel (II) Chelate: X-Ray Crystallographic and DFT Studies," *Polyhedron* 124 (2017): 22–29, https://doi.org/10.1016/j.poly.2016.12.026.

15. J. S. Hart, G. S. Nichol, and J. B. Love, "Directed Secondary Interactions in Transition Metal Complexes of Tripodal Pyrrole Imine and Amide Ligands," *Dalton Transactions* 41 (2012): 5785–5788, https://doi.org/10.1039/C2DT30539A.

16. H. Liang, J. Liu, X. Li, and Y. Li, "Synthesis, Structure and Norbornene Polymerization Behavior of Neutral Palladium Complexes," *Polyhedron* 23 (2004): 1619–1627, https://doi.org/10.1016/j.poly.2004.03.017.

17. C. N. Iverson, C. A. G. Carter, R. T. Baker, J. D. Scollard, J. A. Labinger, and J. E. Bercaw, "C−H Bond Activation by Unsymmetrical 2-(N-Arylimino)Pyrrolide Pt Complexes: Geometric Effects on Reactivity," *Journal of the American Chemical Society* 125 (2003): 12674–12675, https://doi.org/10.1021/ja036511d.

18. X.-F. Shan, D.-H. Wang, C.-H. Tung, and L.-Z. Wu, "C–H···Pt (II) Interaction-Controlled Self-Assembly and Photophysics of Chiral Bis (Pyrrol-2-Ylmethyleneamino)Cyclohexane Platinum (II) Complexes," *Tetrahedron* 64 (2008): 5577–5582, https://doi.org/10.1016/j.tet.2008.03.077.

19. Y. Kim, J. Lee, Y.-H. Son, S.-U. Choi, M. Alam, and S. Park, "Novel Nickel (II), Palladium (II), and Platinum (II) Complexes Having a Pyrrolyl-Iminophosphine (PNN) Pincer: Synthesis, Crystal Structures, and Cytotoxic Activity," *Journal of Inorganic Biochemistry* 205 (2020): 111015, https://doi.org/10.1016/j.jinorgbio.2020.111015.

20. M. A. Rhine, A. V. Rodrigues, R. J. B. Urbauer, J. L. Urbauer, T. L. Stemmler, and T. C. Harrop, "Proton-Induced Reactivity of NO− From a {CoNO}8 Complex," *Journal of the American Chemical Society* 136 (2014): 12560–12563, https://doi.org/10.1021/ja5064444.

21. M. R. Walter, S. P. Dzul, A. V. Rodrigues, et al., "Synthesis of CoII–NO− Complexes and Their Reactivity as a Source of Nitroxyl," *Journal of the American Chemical Society* 138 (2016): 12459–12471, https://doi.org/10.1021/jacs.6b05896.

22. D. Bandyopadhyay, M. Layek, M. Fleck, R. Saha, and C. Rizzoli, "Synthesis, Crystal Structure and Antibacterial Activity of Azido Complexes of Cobalt (III) Containing Heteroaromatic Schiff Bases," *Inorganica Chimica Acta* 461 (2017): 174–182, https://doi.org/10.1016/j.ica.2017.02.018.

23. S. A. Carabineiro, L. C. Silva, P. T. Gomes, et al., "Synthesis and Characterization of Tetrahedral and Square Planar Bis (Iminopyrrolyl)

Complexes of Cobalt (II)," *Inorganic Chemistry* 46 (2007): 6880–6890, https://doi.org/10.1021/ic062125w.

24. H. Brunner, B. Nuber, and T. Tracht, "Optically Active Transition Metal Complexes. Part 119:[1]New Rhodium(I) Complexes Containing Two Different Types of Optically Active Ligands," *Tetrahedron: Asymmetry* 9 (1998): 3763–3771, https://doi.org/10.1016/S0957-4166(98)00389-9.

25. H. Brunner, A. Köllnberger, and M. Zabel, "Optically Active Transition Metal Complexes. Part 133.Preparation, Epimerization and Crystallization of Chiral-at-Metal Rhodium (III) Half-Sandwich Complexes," *Polyhedron* 22 (2003): 2639–2646, https://doi.org/10.1016/S0277-5387(03)00346-2.

26. S. Basu, I. Pal, R. J. Butcher, G. Rosair, and S. Bhattacharya, "Rhodium and Iridium Complexes of N-(2′-Hydroxyphenyl)Pyrrole-2-Aldimine: Synthesis, Structure, and Spectral and Electrochemical Properties," *Journal of Chemical Sciences* 117 (2005): 167–173, https://doi.org/10.1007/BF03356112.

27. Y. Haketa, M. Miyasue, Y. Kobayashi, et al., "Self-Associating Curved π-Electronic Systems With Electron-Donating and Hydrogen-Bonding Properties," *Journal of the American Chemical Society* 142 (2020): 16420–16428, https://doi.org/10.1021/jacs.0c07751.

28. P. Paul, M. G. Richmond, and S. Bhattacharya, "Iridium-Mediated N–H and Methyl C–H Bond Activations in N-(2′,6′-Dimethylphenyl) Pyrrole-2-Aldimine. Synthesis, Characterization and Catalytic Applications," *Journal of Organometallic Chemistry* 751 (2014): 760–768, https://doi.org/10.1016/j.jorganchem.2013.07.066.

29. N. Myeza, C. Slabber, O. Q. Munro, et al., "An 8-Aminoquinoline-Naphthyl Copper Complex Causes Apoptotic Cell Death by Modulating the Expression of Apoptotic Regulatory Proteins in Breast Cancer Cells," *European Journal of Pharmacology* 978 (2024): 176764, https://doi.org/10.1016/j.ejphar.2024.176764.

30. F. Z. C. Fellah, J.-P. Costes, F. Dahan, et al., "Di- and Triheteronuclear Cu–Gd and Cu–Gd–Cu Complexes With Dissymmetric Double Bridge," *Inorganic Chemistry* 47 (2008): 6444–6451, https://doi.org/10.1021/ic800599r.

31. Y. Hu, Q. Li, H. Li, Q. Guo, Y. Lu, and Z. Li, "A Novel Class of Cd (II), Hg (II) Turn-On and Cu (II), Zn (II) Turn-Off Schiff Base Fluorescent Probes," *Dalton Transactions* 39 (2010): 11344–11352, https://doi.org/10.1039/C0DT00737D.

32. H. Adams, M. R. J. Elsegood, D. E. Fenton, S. L. Heath, and S. J. Ryan, "Dinuclear Silver(I) Complexes of Bibracchial Tetraimine Schiff Base Macrocycles Derived From Pyrrole-2,5-Dicarbaldehyde," *Journal of the Chemical Society, Dalton Transactions* no. 12 (1999): 2031–2038, https://doi.org/10.1039/A901992H.

33. K. J. Akerman, A. M. Fagenson, V. Cyril, et al., "Gold (III) Macrocycles: Nucleotide-Specific Unconventional Catalytic Inhibitors of Human Topoisomerase I," *Journal of the American Chemical Society* 136 (2014): 5670–5682, https://doi.org/10.1021/ja412350f.

34. A. Frei, A. D. Verderosa, A. G. Elliott, J. Zuegg, and M. A. Blaskovich, "Metals to Combat Antimicrobial Resistance," *Nature Reviews Chemistry* 7 (2023): 202–224.

35. D. C. Crans and K. Kostenkova, "Open Questions on the Biological Roles of First-Row Transition Metals," *Communications Chemistry* 3 (2020): 104.

36. C. van Cleave and D. C. Crans, "The First-Row Transition Metals in the Periodic Table of Medicine," *Inorganics* 7 (2019): 111.

37. C. M. Curieses Andrés, J. M. Pérez de Lastra, E. Bustamante Munguira, C. Andrés Juan, and E. Pérez-Lebeña, "Anticancer Activity of Metallodrugs and Metallizing Host Defense Peptides—Current Developments in Structure-Activity Relationship," *International Journal of Molecular Sciences* 25, no. 13 (2024): 7314.

38. S. Adhikari, P. Nath, A. Das, et al., "A Review on Metal Complexes and Its Anti-Cancer Activities: Recent Updates From in Vivo Studies," *Biomedicine & Pharmacotherapy* 171 (2024): 116211.

39. T. Nabiyeva, C. Marschner, and B. Blom, "Synthesis, Structure and Anti-Cancer Activity of Osmium Complexes Bearing π-Bound Arene Substituents and Phosphane Co-Ligands: A Review," *European Journal of Medicinal Chemistry* 201 (2020): 112483.

40. G. Kurpik, A. Walczak, M. Gołdyn, J. Harrowfield, and A. R. Stefankiewicz, "Pd (II) Complexes With Pyridine Ligands: Substituent Effects on the NMR Data, Crystal Structures, and Catalytic Activity," *Inorganic Chemistry* 61 (2022): 14019–14029, https://doi.org/10.1021/acs.inorgchem.2c01996.

41. A. I. Osman, A. Ayati, P. Krivoshapkin, et al., "Coordination-Driven Innovations in low-Energy Catalytic Processes: Advancing Sustainability in Chemical Production," *Coordination Chemistry Reviews* 514 (2024): 215900.

42. M. Bashir, A. A. Dar, and I. Yousuf, "Syntheses, Structural Characterization, and Cytotoxicity Assessment of Novel Mn (II) and Zn (II) Complexes of Aroyl-Hydrazone Schiff Base Ligand," *ACS Omega* 8 (2023): 3026–3042, https://doi.org/10.1021/acsomega.2c05927.

43. Z. Puterová-Tokárová, V. Mrázová, and R. Boča, "Magnetism of Novel Schiff-Base Copper (II) Complexes Derived From Aminoacids," *Polyhedron* 61 (2013): 87–93.

44. M. Andruh, "Compartmental Schiff-Base Ligands—A Rich Library of Tectons in Designing Magnetic and Luminescent Materials," *Chemical Communications* 47 (2011): 3025–3042.

45. S. M. Abd El-Hamid, S. A. Sadeek, S. F. Mohammed, F. M. Ahmed, and M. S. El-Gedamy, "N2O2-Chelate Metal Complexes With Schiff Base Ligand: Synthesis, Characterisation and Contribution as a Promising Antiviral Agent Against Human Cytomegalovirus," *Applied Organometallic Chemistry* 37 (2023): e6958, https://doi.org/10.1002/aoc.6958.

46. S. K. Pal, A. Krishnan, P. K. Das, and A. G. Samuelson, "Schiff Base Linked Ferrocenyl Complexes for Second-Order Nonlinear Optics," *Journal of Organometallic Chemistry* 604 (2000): 248–259.

47. C.-G. Liu, Y.-Q. Qiu, S.-L. Sun, H. Chen, N. Li, and Z.-M. Su, "DFT Study on Second-Order Nonlinear Optical Properties of a Series of Mono Schiff-Base M (II)(M= Ni, Pd, Pt) Complexes," *Chemical Physics Letters* 429 (2006): 570–574.

48. S. Sookai, S. Perumal, M. Kaur, and O. Q. Munro, "Pt (II) Bis (Pyrrole-Imine) Complexes: Luminescent Probes and Cytotoxicity in MCF-7 Cells," *Journal of Inorganic Biochemistry* 258 (2024): 112617.

49. W. al Zoubi, A. A. S. Al-Hamdani, and M. Kaseem, "Synthesis and Antioxidant Activities of Schiff Bases and Their Complexes: A Review," *Applied Organometallic Chemistry* 30 (2016): 810–817, https://doi.org/10.1002/aoc.3506.

50. S. Y. Lawan, M. B. Mshelia, G. A. Mala, et al., "Antioxidant Activity and DFT Calculations of Metal Complexes Derived From a Schiff Base Ligand: Synthesis, Characterization, and Biological Evaluation," *ChemistrySelect* 9 (2024): e202400676, https://doi.org/10.1002/slct.202400676.

51. T. A. Martin and W. G. Jiang, "Anti-Cancer Agents in Medicinal Chemistry (Formerly Current Medicinal Chemistry-Anti-Cancer Agents)," *Anti-Cancer Agents in Medicinal Chemistry* 10 (2010): 1.

52. K. T. Tadele and T. W. Tsega, "Schiff Bases and Their Metal Complexes as Potential Anticancer Candidates: A Review of Recent Works," *Anti-Cancer Agents in Medicinal Chemistry (Formerly Current Medicinal Chemistry-Anti-Cancer Agents)* 19 (2019): 1786–1795.

53. S. Sookai, M. P. Akerman, and O. Q. Munro, "Chiral Au(Iii) Chelates Exhibit Unique NCI-60 Cytotoxicity Profiles and Interactions With Human Serum Albumin," *Dalton Transactions* 53 (2024): 5089–5104, https://doi.org/10.1039/D3DT04024K.

54. A. Catalano, M. S. Sinicropi, D. Iacopetta, et al., "A Review on the Advancements in the Field of Metal Complexes With Schiff Bases as Antiproliferative Agents," *Applied Sciences* 11 (2021): 6027.

55. M. Yadav, D. Yadav, D. P. Singh, and J. K. Kapoor, "Pharmaceutical Properties of Macrocyclic Schiff Base Transition Metal Complexes: Urgent Need in Today's World," *Inorganica Chimica Acta* 546 (2023): 121300.

56. J. M. Mir, S. A. Majid, and A. H. Shalla, "Enhancement of Schiff Base Biological Efficacy by Metal Coordination and Introduction of Metallic Compounds as Anticovid Candidates: A Simple Overview," *Reviews in Inorganic Chemistry* 41 (2021): 199–211, https://doi.org/10.1515/revic-2020-0020.

57. P. Durairaj, T. Maruthavanan, S. Manjunathan, S. Subashini, S. L. Rokhum, and G. Baskar, "Microwave Assisted Synthesis, Characterization and Bioactivity Evaluation of a Cobalt (II) Complex With a Novel Schiff Base Ligand Derived From Phenylacetyl Urea and Salicylaldehyde," *Journal of Molecular Structure* 1295 (2024): 136650, https://doi.org/10.1016/j.molstruc.2023.136650.

58. T. L. Yusuf, I. Waziri, K. A. Olofinsan, E. O. Akintemi, E. C. Hosten, and A. J. Muller, "Evaluating the In Vitro Antidiabetic, Antibacterial and Antioxidant Properties of Copper (II) Schiff Base Complexes: An Experimental and Computational Studies," *Journal of Molecular Liquids* 389 (2023): 122845, https://doi.org/10.1016/j.molliq.2023.122845.

59. L. A. Alfonso-Herrera, D. Hernández-Romero, J. A. Cruz-Navarro, et al., "Transition Metal Complexes With Tetradentate Schiff Bases (N2O2) Obtained From Salicylaldehyde: A Review of Their Possible Anticancer Properties," *Coordination Chemistry Reviews* 505 (2024): 215698, https://doi.org/10.1016/j.ccr.2024.215698.

60. A. C. Pinheiro, I. J. Nunes, W. V. Ferreira, et al., "Antioxidant and Anticancer Potential of the New Cu (II) Complexes Bearing Imine-Phenolate Ligands With Pendant Amine N-Donor Groups," *Pharmaceutics* 15 (2023): 376, https://doi.org/10.3390/pharmaceutics15020376.

61. T. S. Lange, K. K. Kim, R. K. Singh, R. M. Strongin, C. K. McCourt, and L. Brard, "Iron (III)-Salophene: An Organometallic Compound With Selective Cytotoxic and Anti-Proliferative Properties in Platinum-Resistant Ovarian Cancer Cells," *PLoS ONE* 3 (2008): e2303, https://doi.org/10.1371/journal.pone.0002303.

62. M.-J. Li, T.-Y. Lan, Z.-S. Lin, C. Yi, and G.-N. Chen, "Synthesis, Characterization, and DNA Binding of a Novel Ligand and Its Cu (II) Complex," *Journal of Biological Inorganic Chemistry* 18 (2013): 993–1003, https://doi.org/10.1007/s00775-013-1048-7.

63. D. Śmiłowicz and N. Metzler-Nolte, "Bioconjugates of Co (III) Complexes With Schiff Base Ligands and Cell Penetrating Peptides: Solid Phase Synthesis, Characterization and Antiproliferative Activity," *Journal of Inorganic Biochemistry* 206 (2020): 111041, https://doi.org/10.1016/j.jinorgbio.2020.111041.

64. M. Asadi, S. B. Sadi, Z. Asadi, R. Yousefi, A. R. Barzegar Sadi, and H. Khalili-Hezarjaribi, "Synthesis, Characterization, and Thermodynamic Studies of the Interaction of Some New Water-Soluble Schiff-Base Complexes with Bovine Serum Albumin," *Journal of Coordination Chemistry* 65 (2012): 722–739, https://doi.org/10.1080/00958972.2012.661419.

65. Ö. Özdemir, P. Gürkan, Y. D. Şimay Demir, and M. Ark, "Novel Palladium (II) Complexes of *N*-(5-Nitro-Salicylidene)-Schiff Bases: Synthesis, Spectroscopic Characterization and Cytotoxicity Investigation," *Journal of Molecular Structure* 1207 (2020): 127852, https://doi.org/10.1016/j.molstruc.2020.127852.

66. C. M. C. Andrés, J. M. Pérez de la Lastra, E. Bustamante Munguira, C. Andrés Juan, and E. Pérez-Lebeña, "Michael Acceptors as Anti-Cancer Compounds: Coincidence or Causality?," *International Journal of Molecular Sciences* 25 (2024): 6099, https://doi.org/10.3390/ijms25116099.

67. A. Dhiman, R. Sharma, and R. K. Singh, "Target-Based Anticancer Indole Derivatives and Insight Into Structure–Activity Relationship: A Mechanistic Review Update (2018–2021)," *Acta Pharmaceutica Sinica B* 12 (2022): 3006–3027, https://doi.org/10.1016/j.apsb.2022.03.021.

68. J. Devi, M. Yadav, D. Kumar, L. S. Naik, and D. K. Jindal, "Some Divalent Metal (II) Complexes of Salicylaldehyde-Derived Schiff Bases: Synthesis, Spectroscopic Characterization, Antimicrobial and In Vitro Anticancer Studies," *Applied Organometallic Chemistry* 33 (2019): e4693, https://doi.org/10.1002/aoc.4693.

69. G. Venkatesh, P. Vennila, S. Kaya, et al., "Synthesis and Spectroscopic Characterization of Schiff Base Metal Complexes, Biological Activity, and Molecular Docking Studies," *ACS Omega* 9 (2024): 8123–8138, https://doi.org/10.1021/acsomega.3c08526.

70. D. K. Mishra, U. K. Singha, A. Das, et al., "DNA Binding, Amelioration of Oxidative Stress, and Molecular Docking Study of Zn (II) Metal Complex of a New Schiff Base Ligand," *Journal of Coordination Chemistry* 71 (2018): 2165–2182, https://doi.org/10.1080/00958972.2018.1476687.

71. I. Waziri, T. L. Yusuf, E. Akintemi, M. T. Kelani, and A. Muller, "Spectroscopic, Crystal Structure, Antimicrobial and Antioxidant Evaluations of New Schiff Base Compounds: An Experimental and Theoretical Study," *Journal of Molecular Structure* 1273 (2023): 134382, https://doi.org/10.1016/j.molstruc.2022.134382.

72. I. Waziri, T. L. Yusuf, H. A. Zarma, S. O. Oselusi, L.-C. C. Coetzee, and A. S. Adeyinka, "New Palladium (II) Complexes From Halogen Substituted Schiff Base Ligands: Synthesis, Spectroscopic, Biological Activity, Density Functional Theory, and Molecular Docking Investigations," *Inorganica Chimica Acta* 552 (2023): 121505.

73. T. Lewis Yusuf, D. Caleb Akintayo, S. Daniel Oladipo, et al., "The Effect of Structural Configuration on the DNA Binding and in Vitro Antioxidant Properties of New Copper(Ii) N 2 O 2 Schiff Base Complexes," *New Journal of Chemistry* 46 (2022): 12968–12980, https://doi.org/10.1039/D2NJ01477G.

74. T. L. Yusuf, S. D. Oladipo, S. Zamisa, et al., "Design of New Schiff-Base Copper (II) Complexes: Synthesis, Crystal Structures, DFT Study, and Binding Potency Toward Cytochrome P450 3A4," *ACS Omega* 6 (2021): 13704–13718, https://doi.org/10.1021/acsomega.1c00906.

75. S. A. Olagboye, T. L. Yusuf, S. D. Oladipo, and S. J. Zamisa, "Crystal Structure of Bis(2-Hydroxy-6-((Phenylimino)Methyl)Phenolato-κ2N,O)Copper (II), C26H20CuN2O4," *Zeitschrift für Kristallographie - New Crystal Structures* 235 (2020): 689–692, https://doi.org/10.1515/ncrs-2019-0900.

76. D. van der Westhuizen, D. I. Bezuidenhout, and O. Q. Munro, "Cancer Molecular Biology and Strategies for the Design of Cytotoxic Gold(I) and Gold(III) Complexes: A Tutorial Review," *Dalton Transactions* 50 (2021): 17413–17437, https://doi.org/10.1039/D1DT02783B.

77. E. Alessio, "Thirty Years of the Drug Candidate NAMI-A and the Myths in the Field of Ruthenium Anticancer Compounds: A Personal Perspective," *European Journal of Inorganic Chemistry* 2017 (2017): 1549–1560, https://doi.org/10.1002/ejic.201600986.

78. K. Andiappan, A. Sanmugam, E. Deivanayagam, K. Karuppasamy, H.-S. Kim, and D. Vikraman, "In Vitro Cytotoxicity Activity of Novel Schiff Base Ligand–Lanthanide Complexes," *Scientific Reports* 8 (2018): 3054, https://doi.org/10.1038/s41598-018-21366-1.

79. L. Yin, S. Zhang, T. Zhou, H. Zhen'guang, and S. Zhang, "Synthesis, Characterization, and Anticancer Activity of Mononuclear Schiff-Base Metal Complexes," *Journal of Molecular Structure* 1275 (2023): 134683, https://doi.org/10.1016/j.molstruc.2022.134683.

80. D. Sinha, A. K. Tiwari, S. Singh, et al., "Synthesis, Characterization and Biological Activity of Schiff Base Analogues of Indole-3-Carboxaldehyde," *European Journal of Medicinal Chemistry* 43 (2008): 160–165.

81. N.-T. Chen, C.-Y. Wu, C.-Y. Chung, et al., "Probing the Dynamics of Doxorubicin-DNA Intercalation During the Initial Activation of Apoptosis by Fluorescence Lifetime Imaging Microscopy (FLIM)," (2012).

82. E. U. Kurz, P. Douglas, and S. P. Lees-Miller, "Doxorubicin Activates ATM-Dependent Phosphorylation of Multiple Downstream Targets in Part Through the Generation of Reactive Oxygen Species," *Journal of Biological Chemistry* 279 (2004): 53272–53281.

83. D. Bagchi, M. Bagchi, E. A. Hassoun, and S. J. Stohs, "In Vitro and In Vivo Generation of Reactive Oxygen Species, DNA Damage and Lactate Dehydrogenase Leakage by Selected Pesticides," *Toxicology* 104 (1995): 129–140, https://doi.org/10.1016/0300-483X(95)03156-A.

84. D. Hernández-Romero, S. Rosete-Luna, A. López-Monteon, et al., "First-Row Transition Metal Compounds Containing Benzimidazole Ligands: An Overview of Their Anticancer and Antitumor Activity," *Coordination Chemistry Reviews* 439 (2021): 213930, https://doi.org/10.1016/j.ccr.2021.213930.

85. D. M. Kendig and J. B. Tarloff, "Inactivation of Lactate Dehydrogenase by Several Chemicals: Implications for In Vitro Toxicology Studies," *Toxicology In Vitro* 21 (2007): 125–132, https://doi.org/10.1016/j.tiv.2006.08.004.

86. K. Yao, N. Wang, J. Zhuang, et al., "Studies on the Effects of Al (III) on the Lactate Dehydrogenase Activity by Differential Pulse Voltammetry," *Talanta* 73 (2007): 529–533, https://doi.org/10.1016/j.talanta.2007.04.025.

87. S. Goutelle, M. Maurin, F. Rougier, et al., "The Hill Equation: A Review of Its Capabilities in Pharmacological Modelling," *Fundamental & Clinical Pharmacology* 22 (2008): 633–648.

88. B. H. Geierstanger and D. E. Wemmer, "Complexes of the Minor Groove of DNA," *Annual Review of Biophysics and Biomolecular Structure* 24 (1995): 463–493.

89. P. E. Pjura, K. Grzeskowiak, and R. E. Dickerson, "Binding of Hoechst 33258 to the Minor Groove of B-DNA," *Journal of Molecular Biology* 197 (2007): 257–271.

90. N. Shahabadi, S. Kashanian, and F. Darabi, "DNA Binding and DNA Cleavage Studies of a Water Soluble Cobalt (II) Complex Containing Dinitrogen Schiff Base Ligand: The Effect of Metal on the Mode of Binding," *European Journal of Medicinal Chemistry* 45 (2010): 4239–4245, https://doi.org/10.1016/j.ejmech.2010.06.020.

91. K. S. Karumban, R. Raut, P. Gupta, et al., "Mononuclear Cobalt (II) Complexes With Polypyridyl Ligands: Synthesis, Characterization, DNA Interactions and in Vitro Cytotoxicity Towards Human Cancer Cells," *Journal of Inorganic Biochemistry* 233 (2022): 111866, https://doi.org/10.1016/j.jinorgbio.2022.111866.

92. Q. Sun, J. Lu, J.-L. Li, et al., "Synthesis, Crystal Structures, DNA Binding and Cleavage Properties and Protein Binding Activities of Three Mononuclear Cobalt (II) Complexes," *Applied Organometallic Chemistry* 28 (2014): 259–266, https://doi.org/10.1002/aoc.3118.

93. M. Vorlícková, "Conformational Transitions of Alternating Purine-Pyrimidine DNAs in Perchlorate Ethanol Solutions," *Biophysical Journal* 69 (1995): 2033–2043.

94. J. Kypr and M. Vorlíčková, "Circular Dichroism Spectroscopy Reveals Invariant Conformation of Guanine Runs in DNA," *Biopolymers: Original Research on Biomolecules* 67 (2002): 275–277.

95. M. Vorlícková, I. Kejnovská, J. Kovanda, and J. Kypr, "Conformational Properties of DNA Strands Containing Guanine-Adenine and Thymine-Adenine Repeats," *Nucleic Acids Research* 26 (1998): 1509–1514.

96. E. Froehlich, J. S. Mandeville, C. M. Weinert, L. Kreplak, and H. A. Tajmir-Riahi, "Bundling and Aggregation of DNA by Cationic Dendrimers," *Biomacromolecules* 12 (2011): 511–517.

97. B. Nordén and T. Kurucsev, "Analysing DNA Complexes by Circular and Linear Dichroism," *Journal of Molecular Recognition* 7 (1994): 141–155.

98. S. Sookai, M. Akerman, M. Færch, Y. Sayed, and O. Q. Munro, "Cytotoxic Pyrrole-Based Gold (III) Chelates Target Human Topoisomerase II as Dual-Mode Inhibitors and Interact With Human Serum Albumin," *European Journal of Medicinal Chemistry* 287 (2025): 117330.

99. M. A. Galindo, D. Olea, M. A. Romero, et al., "Design and Non-Covalent DNA Binding of Platinum (II) Metallacalix[4]Arenes," *Chemistry – A European Journal* 13 (2007): 5075–5081, https://doi.org/10.1002/chem.200601581.

100. S. Sookai, A. Majoka, M. A. Fernandes, and M. Nowakowska, "Binding Thermodynamics of 1,3-Bis(((E-1H-Pyrrol-2-Yl) Methylene) Amino) Propan-2-Ol Palladium (II) With HSA and Its Intercalative Behaviour in ctDNA," *Journal of Molecular Structure* 1334 (2025): 141880, https://doi.org/10.1016/j.molstruc.2025.141880.

101. H. Rozenberg, D. Rabinovich, F. Frolow, R. S. Hegde, and Z. Shakked, "Structural Code for DNA Recognition Revealed in Crystal Structures of Papillomavirus E2-DNA Targets," *Proceedings. National Academy of Sciences. United States of America* 95 (2018): 15194–15199, https://doi.org/10.1073/pnas.95.26.15194.

102. H. Song, J. T. Kaiser, and J. K. Barton, "Crystal Structure of Δ-[Ru (Bpy) 2 Dppz] 2+ Bound to Mismatched DNA Reveals Side-By-Side Metalloinsertion and Intercalation," *Nature Chemistry* 4 (2012): 615–620.

103. M. Bisht, I. Jha, and P. Venkatesu, "Comprehensive Evaluation of Biomolecular Interactions Between Protein and Amino Acid Based-Ionic Liquids: A Comparable Study Between [Bmim][Br] and [Bmim][Gly] Ionic Liquids," *ChemistrySelect* 1 (2016): 3510–3519, https://doi.org/10.1002/slct.201600524.

104. G. L. Warren, C. W. Andrews, A.-M. Capelli, et al., "A Critical Assessment of Docking Programs and Scoring Functions," *Journal of Medicinal Chemistry* 49 (2006): 5912–5931, https://doi.org/10.1021/jm050362n.

105. V. Salmaso and S. Moro, "Bridging Molecular Docking to Molecular Dynamics in Exploring Ligand-Protein Recognition Process: An Overview," *Frontiers in Pharmacology* 9 (2018): 923, https://doi.org/10.3389/fphar.2018.00923.

106. M. P. O'Hagan, S. Haldar, J. C. Morales, A. J. Mulholland, and M. C. Galan, "Enhanced Sampling Molecular Dynamics Simulations Correctly Predict the Diverse Activities of a Series of Stiff-Stilbene G-Quadruplex DNA Ligands," *Chemical Science* 12 (2021): 1415–1426.

Supporting Information

Additional supporting information can be found online in the Supporting Information section.